ADVANCED MATERIALS
www.advmat.de

Quasi-Binary Transition Metal Dichalcogenide Alloys: Thermodynamic Stability Prediction, Scalable Synthesis, and Application

Zahra Hemmat, John Cavin, Alireza Ahmadiparidari, Alexander Ruckel, Sina Rastegar, Saurabh N. Misal, Leily Majidi, Khagesh Kumar, Shuxi Wang, Jinglong Guo, Radwa Dawood, Francisco Lagunas, Prakash Parajuli, Anh Tuan Ngo, Larry A. Curtiss, Sung Beom Cho, Jordi Cabana, Robert F. Klie, Rohan Mishra, and Amin Salehi-Khojin**

Transition metal dichalcogenide (TMDCs) alloys could have a wide range of physical and chemical properties, ranging from charge density waves to superconductivity and electrochemical activities. While many exciting behaviors of unary TMDCs have been demonstrated, the vast compositional space of TMDC alloys has remained largely unexplored due to the lack of understanding regarding their stability when accommodating different cations or chalcogens in a single-phase. Here, a theory-guided synthesis approach is reported to achieve unexplored quasi-binary TMDC alloys through computationally predicted stability maps. Equilibrium temperature–composition phase diagrams using first-principles calculations are generated to identify the stability of 25 quasi-binary TMDC alloys, including some involving non-isovalent cations and are verified experimentally through the synthesis of a subset of 12 predicted alloys using a scalable chemical vapor transport method. It is demonstrated that the synthesized alloys can be exfoliated into 2D structures, and some of them exhibit: i) outstanding thermal stability tested up to 1230 K, ii) exceptionally high electrochemical activity for the CO_2 reduction reaction in a kinetically limited regime with near zero overpotential for CO formation, iii) excellent energy efficiency in a high rate Li–air battery, and iv) high break-down current density for interconnect applications. This framework can be extended to accelerate the discovery of other TMDC alloys for various applications.

As a class of 2D materials, transition metal dichalcogenides (TMDCs) display diverse physical properties, including topological insulator properties,[1,2] superconductivity,[3–6] valley polarization,[7–10] and enhanced electrocatalytic activity for various chemical reactions.[11–18] This diversity arises due to the ability of TMDCs to accommodate different transition-metal elements, such as Mo, W, V, Nb, Ta, Re and others, with the three chalcogens (S, Se, and Te) in stable layered structures—that can be exfoliated to a desired number of 2D layers to control quantum confinement. Their properties can be further tuned—or even new properties engineered—by alloying two different elements at either the transition metal or the chalcogen site[19–26] to form quasi-binary alloys, or by simultaneous alloying at both the sites to form quaternary alloys.[17,21,27,28] Thus far, quasi-binary alloys of semiconducting TMDCs, such as $Mo_{(1-x)}W_xS_2$, $Mo_{(1-x)}W_xSe_2$, $MoS_{2(1-x)}Se_{2x}$, and $WS_{2(1-x)}Se_{2x}$, have garnered the most

Z. Hemmat, A. Ahmadiparidari, S. Rastegar, S. N. Misal, L. Majidi, Prof. A. Salehi-Khojin
Department of Mechanical and Industrial Engineering
University of Illinois
Chicago, IL 60607, USA
E-mail: salehikh@uic.edu

J. Cavin
Department of Physics
Washington University
St. Louis, MO 63130, USA

A. Ruckel, S. Wang, J. Guo, R. Dawood, F. Lagunas, Dr. P. Parajuli, Prof. R. F. Klie
Department of Physics
University of Illinois
Chicago, IL 60607, USA

The ORCID identification number(s) for the author(s) of this article can be found under https://doi.org/10.1002/adma.201907041.

DOI: 10.1002/adma.201907041

K. Kumar, Prof. J. Cabana
Department of Chemistry
University of Illinois at Chicago
Chicago, IL 60607, USA

Dr. A. T. Ngo, Dr. L. A. Curtiss
Materials Science Division
Argonne National Laboratory
Argonne, IL 60439, USA

Dr. S. B. Cho, Prof. R. Mishra
Department of Mechanical Engineering and Material Science
Washington University
St. Louis, MO 63130, USA
E-mail: rmishra@wustl.edu

Prof. R. Mishra
Institute of Materials Science and Engineering
Washington University
St. Louis, MO 63130, USA

attention as they allow tuning of the bandgap.[20,22–26,29–32] In a few other cases, alloying leads to more drastic changes to the crystal structure and electronic properties, for example, the triggering of a metal-to-semiconductor transition by alloying $MoTe_2$ with WTe_2.[33] Theoretical predictions based on first-principles methods provide further impetus for realizing new TMDC alloys by showing the possibility to achieve materials with not only enhanced electronic and optical properties but new properties, such as magnetism.[33–38]

Despite their promise, experimental demonstration of TMDC alloys, especially those involving non-isovalent cations, has been limited. This is primarily due to lack of knowledge regarding the stability of the alloys under relevant growth conditions, which subjects their successful synthesis to a trial-and-error based process. In this work, first-principles density-functional-theory (DFT) calculations were used to evaluate the stability of 25 alloys including monolayer group V and intergroup V and VI transition-metal-site TMDC alloys as well as chalcogen-site TMDC alloys with group V and VI transition metals. We attempted growth of a subset of 12 TMDC alloys, performed extensive characterization of the structure and composition of the synthesized materials from microscale to the atomic scale and revealed excellent consistency with the theoretical predictions. The chemical formula of the TM- and chalcogen-site alloys have the form $M_{1-x}M'_xX_2$ and $MX_{2(1-x)}X'_{2x}$, respectively, with M, M' = Mo, W, V, Nb, Ta and X, X' = S, Se. Table S1 in the Supporting Information lists all 25 alloys with 20 TM-site alloys—2 group VI alloys, 6 group V alloys, and 12 intergroup alloys—and 5 chalcogen-site alloys. As all the 10 endmember TMDCs being alloyed are stable in the *2H* phase (see Table S2, Supporting Information), we calculated the stability of all the quasi-binary alloys in the same phase. To verify this assumption, we repeated calculations in the *1T* phase for three example alloys and confirmed that the *2H* phase is the ground state. To discern between miscible alloys—that favor random solid solutions over phase segregation at any temperature—from immiscible ones, we calculated their enthalpy of mixing (ΔH_{mix}). The sign of the mixing enthalpy determines the miscibility of the alloy: negative and positive mixing enthalpies correspond, respectively, to energetically favorable and unfavorable mixing conditions at 0 K. The four group VI TMDC alloys—two TM-site, $Mo_{1-x}W_xS_2$ and $Mo_{1-x}W_xSe_2$, and two chalcogen site, $MoS_{2(1-x)}Se_{2x}$ and $MoS_{2(1-x)}Se_{2x}$—are known to be miscible, as confirmed in this work.[29,30] In addition, we discovered the four group V quasi-binary alloys, $Nb_{1-x}Ta_xS_2$, $Nb_{1-x}Ta_xSe_2$, $VS_{2(1-x)}Se_{2x}$, and $TaS_{2(1-x)}Se_{2x}$, to be miscible (**Figure 1**A). The mixing enthalpies of all the alloys are plotted in Figures S1–S3, Supporting Information.

For the alloys with positive ΔH_{mix}, synthesis of a single-phase solid solution is still possible. The stability of an alloy is dependent on the change in the free energy of mixing (ΔG_{mix}) as a function of molar concentration. The free energy with respect to the endpoints of an alloy is given by $\Delta G_{mix}(x; T) = \Delta H_{mix}(x) - T\Delta S(x)$. Because entropy ($\Delta S$) is a positive quantity, increasing the temperature causes the free energy to be lowered, stabilizing the alloy (Section S1, Supporting Information). Figure 1B shows the two contributing terms to ΔG, enthalpy ΔH_{mix} and the temperature-dependent $-T\Delta S$ for $W_{1-x}Nb_xS_2$. It is seen that at sufficiently high temperatures, the entropy term dominates, the free energy is reduced, and the alloy is stabilized. Classifying this temperature-dependent stability requires further analysis of the free energy. For a given finite temperature, the molar concentration of an alloy can be divided into three regions: a stable region, a metastable region, and an unstable region. Figure 1C shows the free energy of $W_{1-x}Nb_xS_2$ at the same temperatures corresponding to Figure 1B. The blue and gray pairs of diamonds demark the boundaries between the stable/metastable regions and metastable/stable regions, respectively (Section S1, Supporting Information). Figure 1D shows the equilibrium phase diagram for $W_{1-x}Nb_xS_2$ with colored lines and gray and blue diamonds that correspond to the temperatures and boundary points displayed in Figure 1C. At ≈640 K, the three regions meet, and the alloy is stable at all molar concentrations. This temperature is known as the miscibility temperature. It gives a quantitative metric for the synthesizability of an immiscible alloy. Figure 1E summarizes the miscibility temperatures for all 20 TM-site and 5 chalcogen-site TMDC alloys that we use to predict their formability. The complete equilibrium phase diagrams are shown in Figures S4 and S5, Supporting Information.

To validate the predictions, we have performed alloy synthesis above and below the miscibility temperatures with the expectation that for alloys having a positive ΔH_{mix}, single-phase structures will only be formed above the miscibility temperatures. We selected 9 TM-site and 3 chalcogen-site quasi-binary TMDC alloys for the synthesis. First, $Nb_{1-x}Ta_xS_2$ and $Nb_{1-x}Ta_xSe_2$ which are predicted to be miscible at any temperature and the immiscible alloy of $W_{1-x}Nb_xS_2$ were chosen for the synthesis, perfomed at two different base temperatures of 500 and 1300 K. The synthesis process was performed using a scalable chemical vapor transport (CVT) method. The samples were grown with the chemical composition corresponding to $x = 0.5$. During the growth process, by maintaining the temperature gradient between the source (hot zone) and the growth zone (cold zone), we obtained high-quality millimeter-sized crystals at the cold zone and powders with high crystalline structures at the hot zone. The inset of **Figure 2**A depicts a typical 1 gram of the powder (e.g., $Nb_{1-x}Ta_xS_2$) collected from the hot zone of ampule which was later used for electrochemical experiments. The synthesized materials were characterized with atomic-resolution scanning transmission electron microscopy (STEM), Raman spectroscopy, X-ray photoelectron spectroscopy (XPS), scanning electron microscopy (SEM), X-ray diffraction (XRD), and energy-dispersive X-ray spectroscopy (EDX).

The macroscopic compositions of the synthesized TMDC particles are measured using EDX in an SEM, and the distribution of elemental compositions collected from ≈50–60 flakes are shown for $Nb_{1-x}Ta_xS_2$, $Nb_{1-x}Ta_xSe_2$ and $W_{1-x}Nb_xS_2$ at two different synthesis temperatures (Figure 2A,B, and Figures S12–S14, Supporting Information). We confirm that the desired stoichiometry of $x \approx 0.5$ is achieved for $Nb_{1-x}Ta_xS_2$ and $Nb_{1-x}Ta_xSe_2$ at both 500 and 1300 K, while only the $W_{1-x}Nb_xS_2$ synthesized at 1300 K shows a single-phase averaging $x = 0.5$. When synthesized at 500 K, $W_{1-x}Nb_xS_2$ appears to separate into two endmember phases. This is expected as the predicted miscibility temperature of $W_{1-x}Nb_xS_2$ is ≈640 K (Figure 1D). Furthermore, a wider distribution of concentrations is found in the Nb-dense phase compared to the W-dense phase (Figure 2B), consistent with the

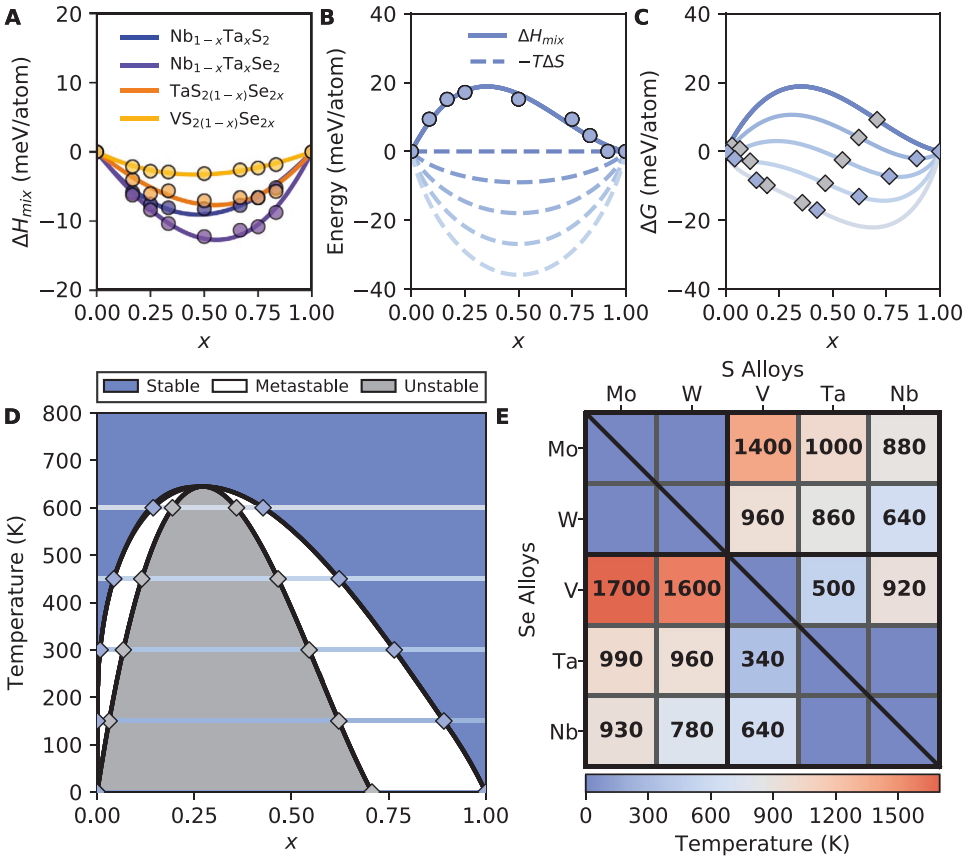

Figure 1. Theoretical predictions of the stability of the TM-site TMDC alloys. A) Negative mixing enthalpies of $Nb_{1-x}Ta_xS_2$, $Nb_{1-x}Ta_xSe_2$, $VS_{2(1-x)}Se_{2x}$, and $TaS_{2(1-x)}Se_{2x}$, the newly predicted miscible alloys. B) DFT-calculated and fitted mixing enthalpy of $W_{1-x}Nb_xS_2$, along with the entropy contribution to the free energy at temperatures between 0 and 600 K in 150 K increments. C) The *x*-dependent free energy of $W_{1-x}Nb_xS_2$ found by adding the enthalpy and entropy terms from (B). The blue and gray diamonds correspond to boundary points between different stability regions in the equilibrium phase diagram. D) The horizontal lines correspond one-to-one in color and temperature with the free energies in (C). E) The miscibility temperatures of all the 20 TM-site TMDC alloys. The top right and bottom left triangles correspond to sulfide and selenide alloys respectively while the diagonal corresponds to chalcogen-site alloys. Dark blue spaces correspond to miscible alloys.

equilibrium phase diagram of $W_{1-x}Nb_xS_2$, which shows a wider region of stability at 500 K on the Nb-dense side (Figure 1D).

Figure 2C,D shows the EDX composition maps for $Nb_{1-x}Ta_xS_2$ and $W_{1-x}Nb_xS_2$, respectively, synthesized at 1300 K, demonstrating that within a single flake, the composition is homogeneous. Atomic-resolution high-angle annular dark-field (HAADF) images from $Nb_{1-x}Ta_xS_2$ and $W_{1-x}Nb_xS_2$, as well as two other alloys of $Mo_{1-x}V_xS_2$ and $MoS_{2(1-x)}Se_{2x}$, are shown in Figure 2E–H. The electron beam diffraction patterns for typical flakes found in the four different TMDCs are shown as insets. The HAADF images and diffraction patterns are obtained for grains in the [001] orientation. The diffraction patterns are labeled according to *2H* phase,[39] which is confirmed by the HAADF images for $Nb_{1-x}Ta_xS_2$ and $W_{1-x}Nb_xS_2$. Moreover, we found that the distribution of Nb and Ta (W and Nb) in $Nb_{1-x}Ta_xS_2$ ($W_{1-x}Nb_xS_2$) appears random, as can be seen by the contrast variations in the HAADF images (Figure 2E,F). Since the image contrast in HAADF images depends directly on the average atomic number of the atomic column being imaged, the variation in the atomic column intensity shown in Figure 2E,F is due to the random mixing of both TM elements. We did not find any sign of preferential segregation in either sample. Furthermore, HAADF imaging cannot distinguish between the *1T* and *2H* phases in the [001] orientation, but the DFT calculations predict that *2H* phase has the lowest formation energy, in agreement with the HAADF image analysis.

These results differ from $Mo_{1-x}V_xS_2$ synthesized at 1300 K (Figure 2G). Here, the EDX elemental analysis, electron diffraction and HAADF imaging show clear signs of phase separation toward MoS_2 and VS_2. The electron diffraction pattern (shown as inset in Figure 2G) also suggests a phase segregation. Figure 2G displays a HAADF image of MoS_2 [001] in the *2H* phase with 1.2% vanadium doping. This doping causes MoS_2 layers within the *2H* $P6_3/mmc$ space group to stack as the *2H* $R3m$ phase. Finally, the HAADF imaging and electron diffraction analysis for $MoS_{2(1-x)}Se_{2x}$ shows a homogeneous distribution of Se and S within the sample. Specifically, the HAADF for $MoS_{2(1-x)}Se_{2x}$ [001], as seen in Figure 2H, shows a nearly constant image intensity of the Mo atomic columns, as expected for the *2H* $P6_3/mmc$ bulk phase. The electron diffraction patterns and HAADF images were also used to determine the lattice parameters for the $Nb_{1-x}Ta_xS_2$, $W_{1-x}Nb_xS_2$, $Mo_{1-x}V_xS_2$

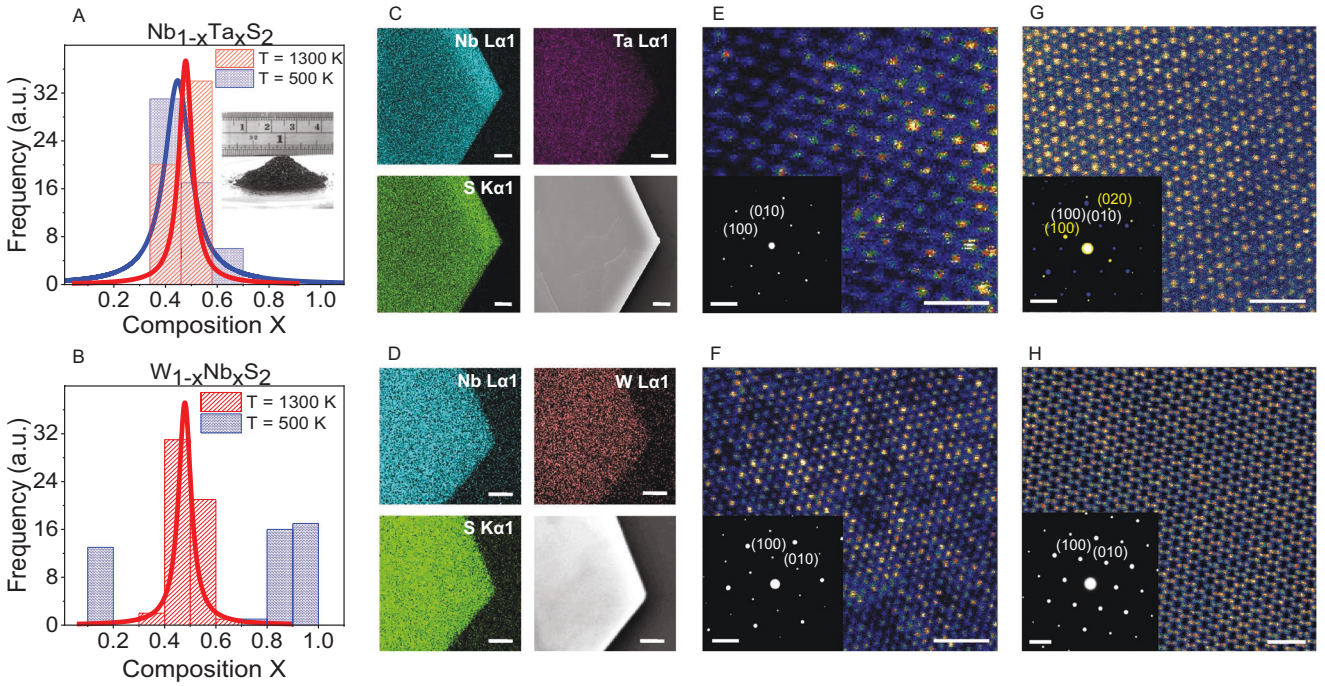

Figure 2. Summary of characterization of $Nb_{1-x}Ta_xS_2$, $W_{1-x}Nb_xS_2$, $Mo_{1-x}V_xS_2$, and $MoS_{2(1-x)}Se_{2x}$ samples selected from 12 synthesized alloys. A,B) EDX frequency distribution of $Nb_{1-x}Ta_xS_2$ and $W_{1-x}Nb_xS_2$ samples grown at the temperature of 500 K (blue) and 1300 K (red). The inset shows the powder collected from the quartz ampoules. C,D) EDX elemental maps obtained from the $Nb_{1-x}Ta_xS_2$ and $W_{1-x}Nb_xS_2$ flakes (scale bars: 1 µm). E,F) Representative atomic-resolution HAADF image of [001] $Nb_{1-x}Ta_xS_2$ and $W_{1-x}Nb_xS_2$ (scale bars: 1 nm), which shows that the transition metal sites are occupied by both elements, and no sign of phase separation is found. Inset contains a selected-area electron diffraction (SAED) pattern labeled according to the *2H* phase (scale bars: 2 nm^{-1}). G,H) Atomic-resolution HAADF image of $Mo_{1-x}V_xS_2$ and $MoS_{2(1-x)}Se_{2x}$ in the [001] orientation (scale bars: 1 nm). The inset shows an SAED pattern (scale bars: 2 nm^{-1}), indexed according to the *2H* phase. While $Mo_{1-x}V_xS_2$ phase-separated into MoS_2 (shown in (G)) and VS_2 (shown in the diffraction pattern only), $MoS_{2(1-x)}Se_{2x}$ appears to be alloyed as expected.

and $MoS_{2(1-x)}Se_{2x}$ samples (see Table S3, Supporting Information). We note that the lattice parameters for all TMDC alloys analyzed here comply with Vegard's Law,[40] where the lattice parameters of the alloys fall between the two endmembers phases, in excellent agreement with the theoretical results (see Figure S6, Supporting Information). Our Raman spectroscopy, XPS, and XRD results also confirm the successful synthesis of these materials and verify their chemical compositions, stoichiometric ratios, and crystallinity (Figures S24–S26, Supporting Information).

To confirm the theoretical predictions for the rest of the selected materials (8 alloys), we synthesized them at 1300 K. In agreement with the theoretical predictions, we observed homogeneous and single-phase structures for $Nb_{1-x}Ta_xSe_2$, $W_{1-x}Nb_xSe_2$, $Mo_{1-x}Nb_xS_2$, $Mo_{1-x}Nb_xSe_2$, $VS_{2(1-x)}Se_{2x}$, $TaS_{2(1-x)}Se_{2x}$, and $V_{1-x}Ta_xS_2$ alloys (Figures S13–S21, Supporting Information). In contrast, for the $Mo_{1-x}V_xSe_2$ alloy, EDX and electron diffraction patterns reveal a phase segregated material due to its high miscibility temperature of 1700 K (Figure S23, Supporting Information).

We tested the thermal stability of all synthesized single-phase materials through thermogravimetric analysis (TGA) (**Figure 3**A). Our results show that $Nb_{1-x}Ta_xS_2$ and $V_{1-x}Ta_xS_2$ retain their structural integrity up to 1230 K with only 3% and 4% weight loss, respectively. At this temperature, $W_{1-x}Nb_xS_2$ shows 10% weight loss while $MoS_{2(1-x)}Se_{2x}$ decomposes completely. All the other alloys exhibit 25–50% weight loss and start to melt and decompose at the temperature range of 600–900 K (Figure 3A). Our results shown in Figure 3B indicate that the thermal stability of $Nb_{1-x}Ta_xS_2$ alloy rivals its unary forms, NbS_2 and TaS_2. Moreover, its thermal stability far exceeds that of the commonly used MoS_2 (Figure 3B). NbS_2 and MoS_2 start to melt at ≈420 and ≈500 K, respectively, leaving sulfur vacancies within the structure (Figures S27–S31, Supporting Information).

These layered materials in their exfoliated mono- and few-layer forms have great potential to be used in a wide range of applications ranging from nanoelectronics to electrochemical energy conversion and storage systems. To explore the exfoliation capability of the synthesized alloys, we have utilized both mechanical and liquid-phase exfoliation techniques. For the liquid-phase exfoliation experiments, the alloys $Nb_{1-x}Ta_xS_2$, $Nb_{1-x}Ta_xSe_2$, and $W_{1-x}Nb_xS_2$ were selected (**Figure 4**A). Details of the exfoliation process are provided in the Experimental Section. Dynamic light scattering (DLS) experiments on exfoliated samples show average lateral sizes of ≈222, ≈199, and ≈130 nm, respectively, for $Nb_{1-x}Ta_xS_2$, $Nb_{1-x}Ta_xSe_2$, and $W_{1-x}Nb_xS_2$ (Figure 4B and Figure S32, Supporting Information). AFM imaging of individual flakes displays typical thicknesses of ≈8 to 22 nm for the synthesized NFs (Figure 4C). AFM height profile distributions of the exfoliated materials obtained from ≈50 randomly selected exfoliated flakes show a well-controlled thickness with an average of about 15–20 nm (Figure 4D). The

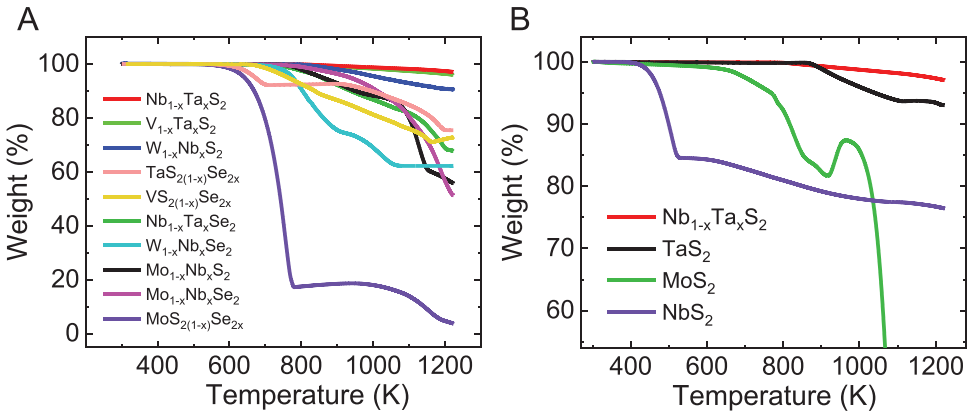

Figure 3. A,B) Thermal gravimetric analysis (TGA) curves for as-synthesized alloys (A) and unary alloys of $Nb_{1-x}Ta_xS_2$ and MoS_2 (B) for structural integrity comparison.

work function results for these three alloys are also shown in Figure S33, Supporting Information.

Next, we studied CO_2 reduction performance of exfoliated $Nb_{1-x}Ta_xS_2$, $Nb_{1-x}Ta_xSe_2$, and $W_{1-x}Nb_xS_2$ nanoflakes as cathode materials and found that $Nb_{1-x}Ta_xS_2$ exhibits the highest activity among tested materials. Its activity is also much higher than that of MoS_2 nanoflakes, as one of the most active catalysts for CO_2 reduction reaction.[12,41] We performed linear sweep voltammetry (LSV) experiments in CO_2 saturated 1 M choline chloride and 1 M KOH solution in a three-electrode setup.[15] Figure 4E shows the LSV results at a very low scan rate of 1 mV s^{-1} (kinetically limited regime) for $Nb_{1-x}Ta_xS_2$ and MoS_2 nanoflakes coated on the gas diffusion layer. The results show a remarkably high current density at –0.8 V versus RHE for $Nb_{1-x}Ta_xS_2$ (–273 mA cm^{-2}), far exceeding that of MoS_2 (–104 mA cm^{-2}). At –0.8 V versus RHE, the obtained current densities for $Nb_{1-x}Ta_xSe_2$ and $W_{1-x}Nb_xS_2$ were –192 and –153 mA cm^{-2}, respectively (Figure S34, Supporting Information). Gas-phase products were analyzed in real-time using differential electrochemical mass spectroscopy (DEMS). DEMS results verify that

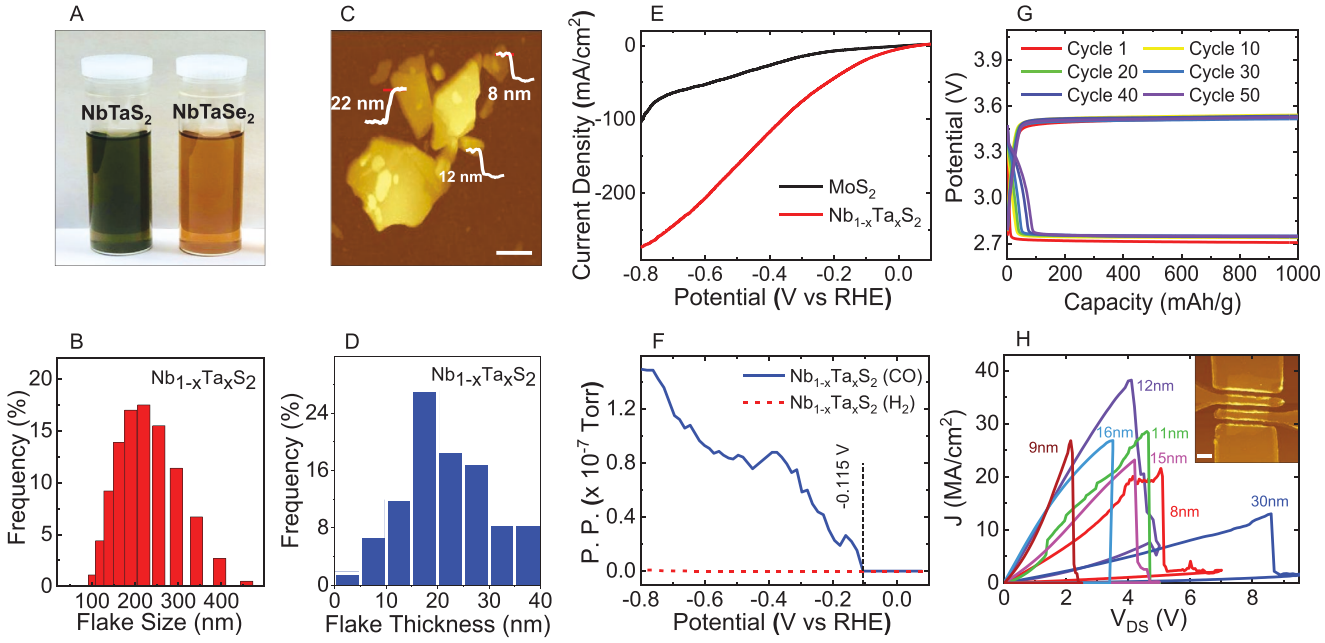

Figure 4. Electrochemical CO_2 reduction, Li–air battery and electrical performance of the $Nb_{1-x}Ta_xS_2$ alloys. A) Dispersions of exfoliated nanoflakes of $Nb_{1-x}Ta_xS_2$ and $Nb_{1-x}Ta_xSe_2$ in IPA solvent. B) Size distribution of synthesized $Nb_{1-x}Ta_xS_2$ alloy obtained by DLS measurements. C) Typical AFM topography image of individual liquid-exfoliated flakes with the heights of 8 and 22 nm (Scale bar: 200 nm). D) Frequency distribution of flake thickness obtained by AFM measurements on ≈50 randomly selected exfoliated flakes. E) LSV results for electrochemical reduction of CO_2 in 1 M choline chloride and 1 M potassium hydroxide using $Nb_{1-x}Ta_xS_2$ (red) and MoS_2 (black) at a scan rate of 1 mV s^{-1}. F) DEMS results for CO (blue) and H_2 (red dotted) production during the LSV experiment using $Nb_{1-x}Ta_xS_2$. CO_2 partial pressure starts to increase at 0.115 V. G) Discharge–charge voltage profiles for 50 cycles operation of Li–air battery. H) Measured current density versus voltage characteristics of $Nb_{1-x}Ta_xS_2$ devices at 300 K approaching high breakdown current density of 40 MA cm^{-2}. The inset shows an AFM image of a four-probe tested structure (Scale bar: 2 μm).

these catalysts are selective toward CO formation rather than H_2 production in the potential window of –0.115 to –0.8 V versus RHE. The onset potential for CO production was found to be –0.115 V versus RHE for $Nb_{1-x}Ta_xS_2$ suggesting a near zero overpotential of 5 mV, which is the smallest overpotential reported for CO_2 reduction so far (Figure 4F).[12,41]

We also examined the catalytic performance of $Nb_{1-x}Ta_xS_2$ in a lithium–air battery system during the discharge and charging processes. Experiments were carried out in a typical Swagelok-type battery cell. The battery consists of a lithium chip as the anode, a glass fiber separator, an electrolyte and $Nb_{1-x}Ta_xS_2$ nanoflakes coated on a gas diffusion layer as the cathode (see the Experimental Section). The electrolyte consists of 0.1 M lithium bis(trifluoromethanesulfonyl)imide (LiTFSI) as the lithium salt and 0.025 M indium iodide (InI_3) as a redox mediator in dimethyl sulfoxide (DMSO) solvent. The battery was operated in a dry air environment at a fixed capacity of 1000 mAh g^{-1} with a high rate of 1000 mA g^{-1}. As shown in Figure 4G, the first discharge and charge curves are observed at ≈2.7 and 3.5 V, respectively. Throughout the battery's operation, there is no significant change in charge and discharge potentials. This indicates an efficient reduction and evolution of oxygen corresponding to the formation and decomposition of Li_2O_2 products (Figures S35 and S36, Supporting Information) during discharging and charging, respectively. We note that the $Nb_{1-x}Ta_xS_2$ catalyst shows a very stable performance in the presence of the redox mediator without any evidence of reduction of triiodide to iodide. Thus, the Li_2O_2 capacity loss was found to be negligible in this battery. The ≈0.7 V polarization gap is one of the smallest values reported so far for Li–air battery systems.

Motivated by the outstanding thermal stability of $Nb_{1-x}Ta_xS_2$, we also investigated the electrical properties of $Nb_{1-x}Ta_xS_2$ for electronic applications. For this purpose, mechanically exfoliated few-layer $Nb_{1-x}Ta_xS_2$ flakes were transferred onto a SiO_2/Si (≈300 nm/0.5 mm) substrate (Figure S37, Supporting Information) and source–drain regions were patterned by electron beam lithography (EBL). Contact metal electrode of Cr/Au (5/50 nm) was deposited followed by standard nanofabrication process (Section S13, Supporting Information). The current–voltage (I_{DS}–V_{DS}) transport characteristics of the tested devices were found to be linear around zero, implying a good Ohmic contact for the channel of the device. The increasing trend of the resistance with increasing temperature verifies the metallic behavior of this material. Also, we observed negligible gate dependency in transfer characteristics (I–V_G) of the tested devices (Figure S38, Supporting Information). Figure 4H represents the breakdown current density versus voltage characteristics of the $Nb_{1-x}Ta_xS_2$ devices measured at 300 K. It is found that $Nb_{1-x}Ta_xS_2$ devices can withstand very high current densities approaching 40 MA cm^{-2}, far larger than typical values reported for the commonly used Cu or Al interconnects (<10 MA cm^{-2}).[42,43] The current density of our multilayered $Nb_{1-x}Ta_xS_2$ (6–20 nm) is among the highest found in multilayered nanomaterials such as TiS_3 nanoribbon (1.7 MA cm^{-2})[44] and multilayer MoS_2 (<1 MA cm^{-2}).[45] It is also comparable with the current density of multilayered graphene (≈40–60 MA cm^{-2}).[44] The limit of current densities for $Nb_{1-x}Ta_xS_2$ devices can be significantly increased by employing encapsulation of the material,[43,46] sandwiched structures,[46] and fabrication of small nanoribbon structures.[43,47] With the growing promise of layered materials,[48–50] the higher current density and thermal stability of $Nb_{1-x}Ta_xS_2$, make it a promising material for high-power electrical interconnects. The (opto)-electronic and electrochemical properties of the other synthesized TMDC alloys remain to be explored in future.

In summary, we report results of a joint theoretical and experimental study on the synthesis of unexplored quasi-binary TMDC alloys with guidance from theoretically predicted stability maps. It is found that certain materials within this grouping exhibit outstanding thermal stability, electrochemical, and electrical properties. Future research will explore other emerging properties of these materials, including superconductivity, magnetic and topological insulator behavior. This study opens up an exciting opportunity to probe the chemical and physical characteristics of other quasi-binary TMDCs and accelerate the discovery of multinary TMDC alloys for various high impact applications.

Experimental Section

Chemical Vapor Transport (CVT) of TMDC Alloys: Before the reaction, quartz ampoules were thoroughly cleaned using diluted HF to remove any organic surface contaminants. Quartz ampoules were rinsed several times with distilled water and annealed at 1300 K for 5 h. The cleaning process for the quartz is necessary as it removes any contamination which interferes with the quality of the crystal. High-purity powders of the transition metals and chalcogens (>99.99% trace metals basis) were mixed in desired stoichiometric proportions and sealed under high vacuum (<10^{-5} Torr) in the ampules. The sealed quartz (with an internal diameter of ≈10 mm and length of ≈15 cm) were placed into a two-zone tube furnace system for the vapor transport growth. To examine the phase stability behavior of the binary alloys, samples were synthesized at two different base growth temperature of 500 and 1300 K. During the high-temperature growth synthesis, both zones of the furnace were heated up to 1300 K with the rate of 50 K h^{-1}. A temperature gradient was established by setting the source material zone (T_{hot}) at 1300 K and the growth zone (T_{cold}) at 1250 K. The system was maintained at this temperature for one week and then gradually cooled down to room temperature at a 50 K h^{-1} rate. However, for the low-temperature growth synthesis, after heating the furnace to 1300 K, the temperature of the hot zone and cold zone were quenched to 500 and 450 K, respectively. The samples were left at this constant temperature for one week and then gradually cooled down to room temperature at a 50 K h^{-1} rate.

Computational Details: Disordered alloys were studied using 6 × 6 supercells of the primitive cell of *2H*-phase TMDCs with molar concentration x = 0.25, 0.50, and 0.75. Additional x values were used for particularly asymmetric alloys and for the four new stable alloys: $Nb_{1-x}Ta_xS_2$, $Nb_{1-x}Ta_xSe_2$, $VS_{2(1-x)}Se_{2x}$, and $TaS_{2(1-x)}Se_{2x}$. To simulate random alloys within small supercells, special quasi-random structures (SQS's) were used.[51] The SQS's were generated using the Alloy Theoretic Automated Toolkit (ATAT).[52] A vacuum spacing of >15 Å was used to reduce the interaction between image planes due to the use of periodic boundary conditions. Total energies were calculated using density-functional theory as implemented in VASP using the Perdew–Burke–Ernzerhof exchange-correlation functional.[53,54] For the large SQS's, geometric relaxation was conducted at only the Γ-point in reciprocal space. A subsequent static calculation for the electronic structure was performed using a Γ-centered 3 × 3 × 1 k-points mesh generated using the Monkhorst–Pack method.[55] Pure TMDCs were studied using a k-points grid of 8 × 8 × 1 for geometry optimization and 24 × 24 × 1 for static calculations. A kinetic energy cutoff of 450 eV was used for all the calculations.

Generating Phase Diagrams: For each alloy, enthalpy values were computed at multiple molar concentration values. These values were fitted to a subregular solution model corresponding to a cubic fit. The change in entropy due to mixing was assumed to be solely from configurational entropy. With functional forms of the enthalpy and entropy, the change in Gibbs free energy was used to determine the boundaries between the different regions of stability at a grid of temperature values, generating an equilibrium phase diagram. See Section S1 in the Supporting Information for more details.

Characterization Techniques: The atomic-resolution scanning transmission electron microscopy (STEM) data was acquired using the aberration-corrected JEOl ARM200CF which is a 200 kV STEM/TEM, equipped with a cold-field emission gun. The high-angle annular dark-field (HAADF) images were acquired using a probe size of 0.078 nm, a convergence semi-angle of 23 mrad, and a collection semi-angle from 68 to 175 mrad.

Scanning electron microscopy (SEM) characterization was carried out using the Raith e-LiNE plus ultra-high-resolution electron beam lithography (EBL) system. Imaging was performed on the cathode by an acceleration voltage (EHT) of 12 kV.

The SEM-EDX measurements were performed with FEI Quanta 650 ESEM integrated with the Oxford AZtec EDS and EBSD systems. The data were obtained in high vacuum with excellent beam stability.

Thermogravimetric analysis (TGA) tests were performed using a TA TGA Q5000 instrument. Samples were loaded onto a platinum high-temperature pan. A heating rate of 25 K min^{-1} was chosen for all specimens, and the temperature range was chosen from room temperature to 1230 K. The nitrogen flow rates for sample and balance were 10 and 25 mL min^{-1}, respectively.

Raman data were obtained with a HORIBA LabRAM HR Evolution confocal Raman microscope equipped with a Horiba Andor detector and 532 nm laser source for excitation. The instrument was configured with a laser spot diameter of ≈1.3 µm, the objective of 50× at laser intensities of less than 7.5 µW $µm^{-2}$. The measurements were performed at room temperature and ambient conditions.

Ultraviolet photoelectron spectroscopy (UPS) and X-ray photoelectron spectroscopy (XPS) data were obtained using a Thermo Scientific ESCALAB 250Xi instrument under high vacuum ($<2 \times 10^{-8}$ mbar). The high-sensitive XPS system was equipped with an electron flood gun and scanning ion gun. Analysis and peak fitting for each element's data was carried out using the Thermo Avantage software.

X-ray diffraction (XRD) was conducted on a Bruker D8 Advance (40 kV, 40 mA) using a Cu Kα (λ_{avg} = 1.5418 Å). The diffraction pattern was recorded from 10° to 75° (2θ).

Dynamic light scattering (DLS) measurements were performed using the Malvern Zetasizer Nano ZLS 380 system equilibrated at 25 °C for 60 s. The instrument equipped with a 10 mW, 633 nm semiconductor laser.

Atomic force microscopy (AFM) topography images were obtained using Bruker Dimension Icon AFM with ScanAsyst-air in tapping mode.

Synthesis of TMDC Alloy Nanoflakes (NFs): TMDC nanoflakes (NFs) were synthesized using a liquid-phase exfoliation method in isopropyl alcohol (IPA) solvent. A mixture of 300 mg of the powder (TMDC alloy) was dispersed in 60 mL IPA solution. The sonication was carried out for 30 h using a probe sonicator (Vibra Cell Sonics 130 W). The resultant dispersions were then centrifuged at high speed (2000 rpm) for 1 h to achieve a supernatant of atomically thin flakes. After centrifugation, the supernatant (roughly the top 70% of the centrifuged solution) was collected for further experiments.

Electrochemical CO_2 Reduction Experiment: 1 M choline chloride/1 M KOH was used as the electrolyte for the electrochemical reduction of CO_2. The solution was purged with CO_2 until it was saturated (pH ≈ 7.60). Linear sweep voltammetry (LSV) experiments were performed at the scan rate of 1 mV s^{-1}. Tested materials were coated on the gas diffusion layer and were used as working electrodes. $Ag/AgNO_3$ and platinum wire (surface area 0.48 cm^2) were used as reference and counter electrodes, respectively. Potentials were converted to RHE using

$$V \text{ versus RHE} = V \text{ versus } Ag/AgNO_3 + 0.155 + 0.0592 \times pH \quad (1)$$

The reported potentials were iR corrected. Gas products from CO_2 reduction were analyzed in real-time using differential electrochemical mass spectroscopy (DEMS) purchased from Hiden Analytical.

Li–Air Battery Experiment: The cathode for the battery experiment was prepared by coating $Nb_{1-x}Ta_xS_2$ nanoflakes on the surface of the gas diffusion layer and the anode, lithium chips (>99.9%), purchased from Sigma-Aldrich. The set-up was assembled in an Ar-filled glove box. The amount of electrolyte immersed in GF/C glass fiber separator was 40 µL. The cycling experiments were carried out by using a potentiostat (MTI- Corporation) with the current density of 1000 mA g^{-1} reaching to 1000 mAh g^{-1} capacity.

Electrical Measurements: To prevent ambient degradation, the $Nb_{1-x}Ta_xS_2$ devices were quickly loaded in a cryogenic probe station under high vacuum environment (chamber pressure = 10^{-8} to 10^{-7} Torr) for electrical measurements. Keithley 2612A System Source Meter was used for applying power to test the current–voltage (I_{DS}–V_{DS}) characteristics of different test structures.

Data and Materials Availability: All data needed to evaluate the conclusions in the paper are present in the paper or in the Supporting Information.

Supporting Information

Supporting Information is available from the Wiley Online Library or from the author.

Acknowledgements

The work of A.S.-K., R.F.K., Z.H., A.A.-P., A.R., S.W., J.G, R.D., F.L., and P.P. are supported by the National Science Foundation DMREF Grant 1729420. A.S.-K., A.T.N, S.R., and L.C. acknowledge the support by the U.S. Department of Energy, Office of Energy Efficiency and Renewable Energy, Vehicle Technologies Office. A.S.-K., J.C., K.K, S.N.M., and L.M. acknowledge the support by the National Science Foundation Grant 1800357. J.C., S.B.C., and R.M. acknowledge support through NSF DMREF-1729787. This work used computational resources of the Extreme Science and Engineering Discovery Environment (XSEDE), which is supported by NSF ACI-1548562. The authors acknowledge the use of the Nanotechnology Core Facility and Electron Microscopy Core of UIC's Research Resources Center. This work made use of the Pritzker Nanofabrication Facility at the University of Chicago and the EPIC and Keck-II facility of Northwestern University's NUANCE Center (DMR-1720139 and NSF ECCS-1542205). The authors thank Dr. Fengyuan Shi for her help with imaging, and TEM-EDS data acquisition.

Conflict of Interest

The authors declare no conflict of interest.

Author Contributions

Z.H. and J.C. contributed equally to this work. A.S.-K. led the material synthesis and electrochemical/thermal/electronic experiments. R.M. led the computational studies. R.F.K. led the microscopy characterizations. Z.H. and A.A.-P. synthesized the TMDC alloys. J.C. and S.B.C. carried out computational studies. Z.H. performed EDX, Raman, and SEM characterizations. A.A.-P. performed TGA. S.R. performed battery experiments. S.N.M. and Z.H. performed the electrochemical experiments. Z.H. and S.W. performed AFM, device nanofabrication and electrical measurements. K.K. performed XRD. L.M. carried out XPS/UPS and DLS experiments. A.R., J.G, P.P., R.D., and F.L. performed the

(S)TEM characterization. L.A.C., A.T.N, S.R., and A.S.-K. conceived the idea for the chemistry of Li–air battery system. All authors contributed to the write up of the manuscript.

Keywords

alloys, CO_2 reduction, density functional theory, phase diagrams, thermal stability, transition metal dichalcogenides

Received: October 27, 2019
Revised: March 12, 2020
Published online: May 25, 2020

[1] E. Sajadi, T. Palomaki, Z. Fei, W. Zhao, P. Bement, C. Olsen, S. Luescher, X. Xu, J. A. Folk, D. H. Cobden, *Science* **2018**, *362*, 922 LP.
[2] X. Qian, J. Liu, L. Fu, J. Li, *Science* **2014**, *346*, 1344 LP.
[3] Y. Saito, T. Nojima, Y. Iwasa, *Nat. Rev. Mater.* **2016**, *2*, 16094.
[4] C. H. Sharma, A. P. Surendran, S. S. Varma, M. Thalakulam, *Commun. Phys.* **2018**, *1*, 90.
[5] E. Navarro-Moratalla, J. O. Island, S. Mañas-Valero, E. Pinilla-Cienfuegos, A. Castellanos-Gomez, J. Quereda, G. Rubio-Bollinger, L. Chirolli, J. A. Silva-Guillén, N. Agraït, G. A. Steele, F. Guinea, H. S. J. van der Zant, E. Coronado, *Nat. Commun.* **2016**, *7*, 11043.
[6] X. Xi, Z. Wang, W. Zhao, J.-H. Park, K. T. Law, H. Berger, L. Forró, J. Shan, K. F. Mak, *Nat. Phys.* **2015**, *12*, 139.
[7] P. Nagler, M. V Ballottin, A. A. Mitioglu, F. Mooshammer, N. Paradiso, C. Strunk, R. Huber, A. Chernikov, P. C. M. Christianen, C. Schüller, T. Korn, *Nat. Commun.* **2017**, *8*, 1551.
[8] K. F. Mak, K. He, J. Shan, T. F. Heinz, *Nat. Nanotechnol.* **2012**, *7*, 494.
[9] A. Arora, R. Schmidt, R. Schneider, M. R. Molas, I. Breslavetz, M. Potemski, R. Bratschitsch, *Nano Lett.* **2016**, *16*, 3624.
[10] H. Zeng, J. Dai, W. Yao, D. Xiao, X. Cui, *Nat. Nanotechnol.* **2012**, *7*, 490.
[11] M. Asadi, B. Sayahpour, P. Abbasi, A. T. Ngo, K. Karis, J. R. Jokisaari, C. Liu, B. Narayanan, M. Gerard, P. Yasaei, X. Hu, A. Mukherjee, K. C. Lau, R. S. Assary, F. Khalili-Araghi, R. F. Klie, L. A. Curtiss, A. Salehi-Khojin, *Nature* **2018**, *555*, 502.
[12] M. Asadi, K. Kim, C. Liu, A. V. Addepalli, P. Abbasi, P. Yasaei, P. Phillips, A. Behranginia, J. M. Cerrato, R. Haasch, P. Zapol, B. Kumar, R. F. Klie, J. Abiade, L. A. Curtiss, A. Salehi-Khojin, *Science* **2016**, *353*, 467.
[13] P. Abbasi, M. Asadi, C. Liu, S. Sharifi-Asl, B. Sayahpour, A. Behranginia, P. Zapol, R. Shahbazian-Yassar, L. A. Curtiss, A. Salehi-Khojin, *ACS Nano* **2017**, *11*, 453.
[14] L. Majidi, P. Yasaei, R. E. Warburton, S. Fuladi, J. Cavin, X. Hu, Z. Hemmat, S. B. Cho, P. Abbasi, M. Vörös, L. Cheng, B. Sayahpour, I. L. Bolotin, P. Zapol, J. Greeley, R. F. Klie, R. Mishra, F. Khalili-Araghi, L. A. Curtiss, A. Salehi-Khojin, *Adv. Mater.* **2019**, *31*, 1804453.
[15] M. Asadi, M. H. Motevaselian, A. Moradzadeh, L. Majidi, M. Esmaeilirad, T. V. Sun, C. Liu, R. Bose, P. Abbasi, P. Zapol, A. P. Khodadoust, L. A. Curtiss, N. R. Aluru, A. Salehi-Khojin, *Adv. Energy Mater.* **2019**, *9*, 1803536.
[16] Q. Gong, L. Cheng, C. Liu, M. Zhang, Q. Feng, H. Ye, M. Zeng, L. Xie, Z. Liu, Y. Li, *ACS Catal.* **2015**, *5*, 2213.
[17] Q. Gong, S. Sheng, H. Ye, N. Han, L. Cheng, Y. Li, *Part. Part. Syst. Charact.* **2016**, *33*, 576.
[18] A. Ahmadiparidari, R. E. Warburton, L. Majidi, M. Asadi, A. Chamaani, J. R. Jokisaari, S. Rastegar, Z. Hemmat, B. Sayahpour, R. S. Assary, B. Narayanan, P. Abbasi, P. C. Redfern, A. Ngo, M. Vörös, J. Greeley, R. Klie, L. A. Curtiss, A. Salehi-Khojin, *Adv. Mater.* **2019**, *31*, 1902518.
[19] H. Li, X. X. Duan, X. Wu, X. Zhuang, H. Zhou, Q. Zhang, X. Zhu, W. Hu, P. Ren, P. Guo, L. Ma, X. Fan, X. Wang, J. Xu, A. Pan, X. X. Duan, *J. Am. Chem. Soc.* **2014**, *136*, 3756.
[20] J. Zhang, S. Jia, I. Kholmanov, L. Dong, D. Er, W. Chen, H. Guo, Z. Jin, V. B. Shenoy, L. Shi, J. Lou, *ACS Nano* **2017**, *11*, 8192.
[21] J. Zhou, J. Lin, X. Huang, Y. Zhou, Y. Chen, J. Xia, H. Wang, Y. Xie, H. Yu, J. Lei, D. Wu, F. Liu, Q. Fu, Q. Zeng, C.-H. Hsu, C. Yang, L. Lu, T. Yu, Z. Shen, H. Lin, B. I. Yakobson, Q. Liu, K. Suenaga, G. Liu, Z. Liu, *Nature* **2018**, *556*, 355.
[22] V. Klee, E. Preciado, D. Barroso, A. E. Nguyen, C. Lee, K. J. Erickson, M. Triplett, B. Davis, I. H. Lu, S. Bobek, J. McKinley, J. P. Martinez, J. Mann, A. A. Talin, L. Bartels, F. Léonard, *Nano Lett.* **2015**, *15*, 2612.
[23] G. Wang, C. Robert, A. Suslu, B. Chen, S. Yang, S. Alamdari, I. C. Gerber, T. Amand, X. Marie, S. Tongay, B. Urbaszek, *Nat. Commun.* **2015**, *6*, 10110.
[24] A. Y. Lu, H. Zhu, J. Xiao, C. P. Chuu, Y. Han, M. H. Chiu, C. C. Cheng, C. W. Yang, K. H. Wei, Y. Yang, Y. Wang, D. Sokaras, D. Nordlund, P. Yang, D. A. Muller, M. Y. Chou, X. Zhang, L. J. Li, *Nat. Nanotechnol.* **2017**, *12*, 744.
[25] Y. Chen, J. Xi, D. O. Dumcenco, Z. Liu, K. Suenaga, D. Wang, Z. Shuai, Y.-S. Huang, L. Xie, *ACS Nano* **2013**, *7*, 4610.
[26] Y. Gong, Z. Liu, A. R. Lupini, G. Shi, J. Lin, S. Najmaei, Z. Lin, A. L. Elías, A. Berkdemir, G. You, H. Terrones, M. Terrones, R. Vajtai, S. T. Pantelides, S. J. Pennycook, J. Lou, W. Zhou, P. M. Ajayan, *Nano Lett.* **2014**, *14*, 442.
[27] S. Susarla, J. A. Hachtel, X. Yang, A. Kutana, A. Apte, Z. Jin, R. Vajtai, J. C. Idrobo, J. Lou, B. I. Yakobson, C. S. Tiwary, P. M. Ajayan, *Adv. Mater.* **2018**, *30*, 1804218.
[28] O. El-Atwani, N. Li, M. Li, A. Devaraj, J. K. S. Baldwin, M. M. Schneider, D. Sobieraj, J. S. Wróbel, D. Nguyen-Manh, S. A. Maloy, E. Martinez, *Sci. Adv.* **2019**, *5*, eaav2002.
[29] J. Kang, S. Tongay, J. Li, J. Wu, *J. Appl. Phys.* **2013**, *113*, 143703.
[30] H.-P. Komsa, A. V Krasheninnikov, *J. Phys. Chem. Lett.* **2012**, *3*, 3652.
[31] S. Tongay, D. S. Narang, J. Kang, W. Fan, C. Ko, A. V. Luce, K. X. Wang, J. Suh, K. D. Patel, V. M. Pathak, J. Li, J. Wu, *Appl. Phys. Lett.* **2014**, *104*, 012101.
[32] M. Zhang, J. Wu, Y. Zhu, D. O. Dumcenco, J. Hong, N. Mao, S. Deng, Y. Chen, Y. Yang, C. Jin, S. H. Chaki, Y.-S. Huang, J. Zhang, L. Xie, *ACS Nano* **2014**, *8*, 7130.
[33] F. Raffone, C. Ataca, J. C. Grossman, G. Cicero, *J. Phys. Chem. Lett.* **2016**, *7*, 2304.
[34] K. Ikeura, H. Sakai, M. S. Bahramy, S. Ishiwata, *APL Mater.* **2015**, *3*, 41514.
[35] P. Yu, J. Lin, L. Sun, Q. L. Le, X. Yu, G. Gao, C.-H. Hsu, D. Wu, T.-R. Chang, Q. Zeng, F. Liu, Q. J. Wang, H.-T. Jeng, H. Lin, A. Trampert, Z. Shen, K. Suenaga, Z. Liu, *Adv. Mater.* **2017**, *29*, 1603991.
[36] Y. Li, K.-A. N. Duerloo, K. Wauson, E. J. Reed, *Nat. Commun.* **2016**, *7*, 10671.
[37] R. Mishra, W. Zhou, S. J. Pennycook, S. T. Pantelides, J.-C. Idrobo, *Phys. Rev. B* **2013**, *88*, 144409.
[38] Y. C. Cheng, Z. Y. Zhu, W. B. Mi, Z. B. Guo, U. Schwingenschlögl, *Phys. Rev. B* **2013**, *87*, 100401.
[39] P. M. Williams, in *Crystallography and Crystal Chemistry of Materials with Layered Structures* (Ed.: F. Lévy), Springer, Dordrecht, The Netherlands **1976**, pp. 51–92.
[40] A. R. Denton, N. W. Ashcroft, *Phys. Rev. A* **1991**, *43*, 3161.
[41] M. Asadi, B. Kumar, A. Behranginia, B. A. Rosen, A. Baskin, N. Repnin, D. Pisasale, P. Phillips, W. Zhu, R. Haasch, R. F. Klie, P. Král, J. Abiade, A. Salehi-Khojin, *Nat. Commun.* **2014**, *5*, 4470.
[42] I. Ames, F. M. d'Heurle, R. E. Horstmann, *IBM J. Res. Dev.* **1970**, *14*, 461.
[43] M. J. Mleczko, R. L. Xu, K. Okabe, H.-H. H. Kuo, I. R. Fisher, H.-S. P. Wong, Y. Nishi, E. Pop, *ACS Nano* **2016**, *10*, 7507.

[44] A. J. Molina-Mendoza, J. O. Island, W. S. Paz, J. M. Clamagirand, J. R. Ares, E. Flores, F. Leardini, C. Sánchez, N. Agraït, G. Rubio-Bollinger, H. S. J. van der Zant, I. J. Ferrer, J. J. Palacios, A. Castellanos-Gomez, *Adv. Funct. Mater.* **2017**, *27*, 1605647.
[45] R. Yang, Z. Wang, P. X.-L. Feng, *Nanoscale* **2014**, *6*, 12383.
[46] J. W. Huang, C. Pan, S. Tran, B. Cheng, K. Watanabe, T. Taniguchi, C. N. Lau, M. Bockrath, *Nano Lett.* **2015**, *15*, 6836.
[47] A. Behnam, A. S. Lyons, M. H. Bae, E. K. Chow, S. Islam, C. M. Neumann, E. Pop, *Nano Lett.* **2012**, *12*, 4424.
[48] Z. Hemmat, P. Yasaei, J. F. Schultz, L. Hong, L. Majidi, A. Behranginia, L. Verger, N. Jiang, M. W. Barsoum, R. F. Klie, A. Salehi-Khojin, *Adv. Funct. Mater.* **2019**, *29*, 1805693.
[49] P. Yasaei, Z. Hemmat, C. J. Foss, S. J. Li, L. Hong, A. Behranginia, L. Majidi, R. F. Klie, M. W. Barsoum, Z. Aksamija, A. Salehi-Khojin, *Adv. Mater.* **2018**, *30*, 1801629.
[50] A. K. Majee, Z. Hemmat, C. J. Foss, A. Salehi-Khojin, Z. Aksamija, *ACS Appl. Mater. Interfaces* **2020**, *12*, 14323.
[51] A. Zunger, S.-H. Wei, L. G. Ferreira, J. E. Bernard, *Phys. Rev. Lett.* **1990**, *65*, 353.
[52] A. van de Walle, M. Asta, G. Ceder, *Calphad* **2002**, *26*, 539.
[53] G. Kresse, J. Furthmüller, *Comput. Mater. Sci.* **1996**, *6*, 15.
[54] J. P. Perdew, K. Burke, M. Ernzerhof, *Phys. Rev. Lett.* **1996**, *77*, 3865.
[55] H. J. Monkhorst, J. D. Pack, *Phys. Rev. B* **1976**, *13*, 5188.